Research Article | Vol. 31, No. 13 / 19 Jun 2023 / Optics Express 21118

Optics EXPRESS

Wavelength-tunable infrared chiral metasurfaces with phase-change materials

HAOTIAN TANG,[1] LILIANA STAN,[2] DAVID A. CZAPLEWSKI,[2] XIAODONG YANG,[1,4] AND JIE GAO[1,3,5]

[1]*Department of Mechanical and Aerospace Engineering, Missouri University of Science and Technology, Rolla, MO 65409, USA*
[2]*Center for Nanoscale Materials, Argonne National Laboratory, Argonne, IL 60439, USA*
[3]*Department of Mechanical Engineering, Stony Brook University, Stony Brook, NY 11794, USA*
[4]*yangxia@mst.edu*
[5]*jie.gao.5@stonybrook.edu*

Abstract: Optical phase-change materials exhibit tunable permittivity and switching properties during phase transition, which offers the possibility of dynamic control of optical devices. Here, a wavelength-tunable infrared chiral metasurface integrated with phase-change material GST-225 is demonstrated with the designed unit cell of parallelogram-shaped resonator. By varying the baking time at a temperature above the phase transition temperature of GST-225, the resonance wavelength of the chiral metasurface is tuned in the wavelength range of 2.33 μm to 2.58 μm, while the circular dichroism in absorption is maintained around 0.44. The chiroptical response of the designed metasurface is revealed by analyzing the electromagnetic field and displacement current distributions under left- and right-handed circularly polarized (LCP and RCP) light illumination. Moreover, the photothermal effect is simulated to investigate the large temperature difference in the chiral metasurface under LCP and RCP illumination, which allows for the possibility of circular polarization-controlled phase transition. The presented chiral metasurfaces with phase-change materials offer the potential to facilitate promising applications in the infrared regime, such as chiral thermal switching, infrared imaging, and tunable chiral photonics.

1. Introduction

Chiral optical structures with the lack of mirror symmetry have the capability of interacting differently with LCP and RCP incident light, which results in circular dichroism (CD) responses [1]. Although chirality plays a critical role in various research fields of drug synthesis [2], chiral sensing [3,4], and optical communication [5,6], the CD in natural optical materials is extremely weak owing to the restricted chiral light-matter interaction strength. On the contrary, optical metasurfaces as artificially engineered materials can possess desirable electromagnetic properties beyond natural materials [7]. In particular, strong chiroptical properties with high CD can be obtained in optical metasurfaces with chiral structures as the unit cells [8]. Recently, chiral metasurfaces have been used as promising candidates in a wide range of advanced applications, such as chiral imaging [9], molecule sensing [10,11] and optical encryption [12]. Nowadays, the evolution of metasurfaces from passive response toward adaptive and active tuning of optical functionalities has been emphasized [13]. Therefore, actively tunable chiral metasurfaces is highly desirable for dynamic control of the chiral wave-matter interactions with circularly polarized light. $Ge_2Sb_2Te_5$ (GST-225) is a non-volatile phase-change material that exhibits exceptional contrast of permittivity during the phase transition from the amorphous to crystalline state [14]. In addition, unlike the volatile phase change material VO_2 [15,16], the non-volatile material does not require continuous energy to maintain the crystalline state. The unique non-volatile permittivity switching feature of GST-225 has led to a wide range of applications of tunable metasurfaces in high-resolution holograms [17,18] and focusing metalenses [19,20]. Meanwhile,

#489841 https://doi.org/10.1364/OE.489841
Journal © 2023 Received 16 Mar 2023; revised 21 Apr 2023; accepted 11 May 2023; published 8 Jun 2023

Optics EXPRESS

optical responses of GST-based metasurfaces can be tuned by phase transition without changing the geometric parameters of the unit-cell structures, showing a great potential in biosensing [21,22], thermal imaging [23], and thermal camouflage [24]. However, the design and study of GST-based chiral metasurfaces have not been reported yet.

In this work, a wavelength-tunable infrared chiral metasurface integrated with phase-change material GST-225 is demonstrated with the designed unit cell of a parallelogram-shaped resonator. The resonance wavelength tuning of chiral metasurfaces is realized through the phase transition of GST-225 material induced by the baking process above the phase transition temperature. The chiral metasurface shows strong absorption close to 0.92 and high CD in absorption around 0.44 across the wavelength tuning range of 2.33 μm to 2.58 μm. The different optical responses of the designed metasurfaces under LCP and RCP illumination are further investigated by studying the distributions of electromagnetic field and displacement current. Finally, the photothermal effect in the chiral metasurface is analyzed to illustrate the temperature difference at the resonance wavelength under LCP and RCP incidence. It implies that temperature in the metasurface can be increased above the GST phase transition temperature due to the strong absorption of LCP light, but below the phase transition temperature with the weak absorption of RCP light, which indicates the possibility of light-induced phase transition controlled by circular polarized incident light. The demonstrated results of tunable infrared chiral metasurfaces will pave the way for the development of dynamically controlled chiral photonic devices to advance applications such as thermal emitters [25], optical switches [26] and optical sensors [27].

2. Design and characterization of tunable chiral metasurfaces

Figure 1(a) displays the schematic of the designed GST-based chiral metasurface, which consists of a 200 nm aluminum mirror deposited on a silicon substrate, a 75 nm GST-225 spacer layer, a 25 nm alumina capping layer, as well as a 60 nm aluminum top layer with parallelogram-shaped resonators. The aluminum layers are deposited using e-beam evaporation. The GST-225 layer is deposited by RF sputtering of a GST-225 target using Ar. The alumina layer is grown by RF sputtering of an Al_2O_3 target. Only Ar gas is used for the first 3 nm to prevent oxidation of the GST-225 and then O_2 is introduced in the chamber to assure the stoichiometry of the Al_2O_3. The top view of the metasurface unit cell is shown in Fig. 1(b), where the horizontal and vertical periods of the unit cell are Px = 1.25 μm and Py = 0.4 μm, respectively. The width of the parallelogram structure is A = 0.24 μm, while the tilted angle of the slot between two neighboring structures is $\alpha = 30°$, and the width of the slot is B = 0.21 μm. The metasurface is fabricated by milling the top aluminum layer using the focused ion beam (FEI Helios Nanolab 600, 30 kV, 24 pA). Figure 1(c) displays a top-view scanning electron microscope (SEM) image of the fabricated metasurface. Aluminum is used as the top resonator and bottom mirror to form a Fabry-Pérot cavity in the metal-dielectric-metal structure, resulting in multiple reflections of the incident light that strongly enhances the optical absorption [28]. The designed metasurface with parallelogram-shaped resonators further allows the selective chiroptical absorption of the incident light with certain circular polarization. In addition, the bottom aluminum mirror layer is thick enough to eliminate the transmitted light so that the absorption (A) of the metasurface can be obtained by characterizing the reflection (R) with A = 1 – R. GST-225 is used as the phase change material in the spacer layer to achieve the tunability of the metasurface, and its thickness is optimized for the desired operation wavelength range. The dynamic tuning of the resonance wavelength of the chiral metasurface can be realized via the change of the permittivity during phase transition. The thin alumina is used as a capping layer on the GST layer to prevent oxidation during the thermally induced phase transition, as well as to reduce the refractive index mismatch between the air and GST layer.

Figure 2(a) illustrates the phase transition from the amorphous state (A) to the crystalline state (C) in GST-225 phase-change material, where the typical phase transition temperature

Optics EXPRESS

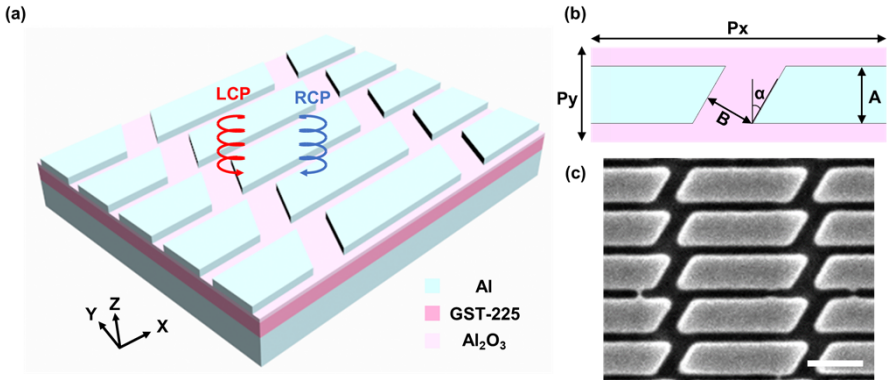

Fig. 1. (a) Schematic diagram of the tunable chiral metasurface with GST-225 phase-change material. (b) Top view of the metasurface unit cell. (c) SEM image of the fabricated chiral metasurface. Scale bar: 500 nm.

is around 393 K [29]. The permittivity of the amorphous and crystalline states of GST-225 in the wavelength range of 2 to 3 μm is plotted in Fig. 2(b), where both the real part (ε1) and imaginary part (ε2) of permittivity show a high contrast before and after the phase transition. It is noted that GST exhibits dielectric responses at both amorphous and crystalline states in infrared wavelength region. The chiroptical responses of the fabricated chiral metasurface are characterized under LCP and RCP incident light. The absorption spectra of the metasurface are obtained by Fourier-transform infrared spectroscopy (FTIR, Nicolet 6700) connected to an infrared microscope, where circularly polarized light is specified by a combination of a broadband linear polarizer and a superachromatic quarter-wave plate (Thorlabs). The CD value in absorption is then obtained by $CD = A_{LCP} - A_{RCP}$. Figure 2(c) plots the measured absorption spectra of the chiral metasurface with GST-225 in the amorphous and crystalline states. Before the phase transition at room temperature, it is clearly shown that a chiral plasmonic resonance located at 2.33 μm has a strong absorption of 0.92 under LCP incidence but a relatively weak absorption of 0.48 under RCP incidence, giving a CD in absorption of 0.44. After heating the metasurface for 15 mins at 408 K (above the phase transition temperature), the chiral plasmonic resonance is red-shifted to approximately 2.58 μm due to the significant increase of the real part of permittivity in GST-225, while the absorption of LCP light remains a high value of 0.91 with a CD in absorption of 0.4. The absorption spectra of the chiral metasurface under LCP and RCP illumination are also simulated using the CST Studio Suite software, where the permittivity values of aluminum and alumina are taken from Refs. [30,31]. The permittivity of GST-225 in Fig. 2(b) is used in the simulation which is obtained from Ref. [32]. The simulated absorption spectra of the chiral metasurface are depicted in Fig. 2(d). It is found that the simulated absorption spectra match well with the measured spectra, when the imaginary part of aluminum permittivity is increased by two times, and the permittivity of GST-225 at partial crystallization condition is considered. The slight deviation between the measured and simulated absorption spectra is attributed to defects and roughness introduced during the FIB milling process.

Geometric parameters including the periods of the unit cell Px and Py, structure width A, slot width B, and the tilted angle α of the slot are optimized to maximize the absorption and chiroptical responses of the metasurface under LCP and RCP incident light. Among these parameters, the tilted angle α of the slot between two neighboring parallelogram resonators plays a critical role in the design. For a symmetrical rectangular structure with $\alpha = 0°$, there is no difference between the absorption of the LCP and RCP light. As α increases, the geometric symmetry of the structure is broken to form the parallelogram chiral structure, which results

Optics EXPRESS

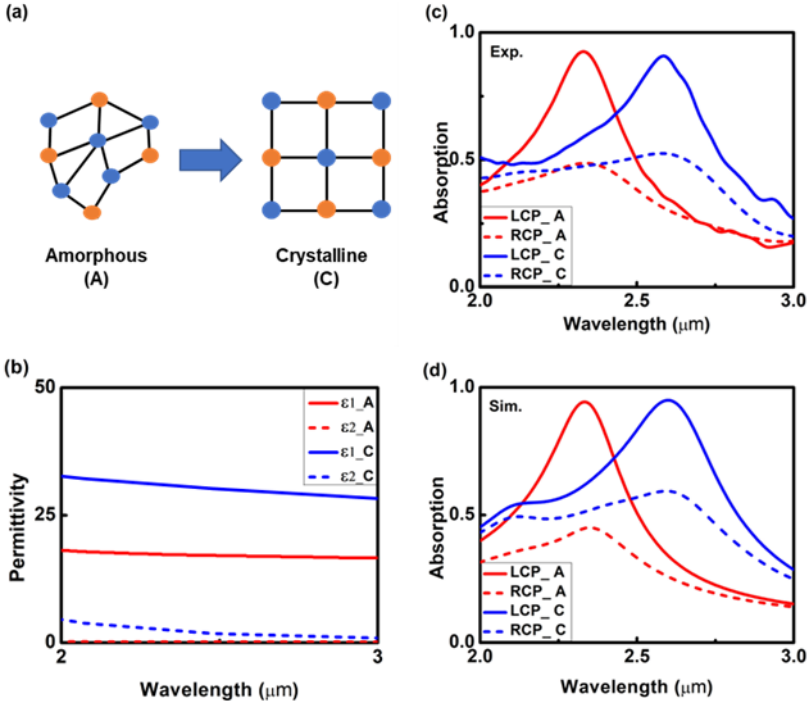

Fig. 2. (a) The illustration of phase transition of GST-225 from the amorphous state to the crystalline state. (b) The real part (ε1) and imaginary part (ε2) of permittivity for GST-225 at the amorphous and crystalline states. (c) Experimentally measured and (d) numerically simulated absorption spectra of the metasurface before and after the phase transition.

in the CD response. Figure 3 shows the simulated spectrum mapping for absorption and CD of the metasurface as the tilted angle of the slot varies from 0° to 60° when GST-225 is at the amorphous and crystalline states. Figures 3(a) and 3(d) indicate the strong absorption is obtained around $\alpha = 30°$ for LCP incidence at both phase states, while there is a significant redshift for the resonance wavelength of the metasurface after the phase transition. However, weak absorption is observed in Figs. 3(b) and 3(e) for RCP incidence for both phase states. As a result, high CD in absorption is reached when the tilted angle of the slot is around 30°~ 50° as shown in Fig. 3(c), and a clear CD spectra shift is also obtained in Fig. 3(f) when GST changes from the amorphous state to the crystalline state.

To further investigate the dynamic tuning process of the GST-based chiral metasurface via the thermally induced phase transition, the absorption spectra of the metasurface are measured during the crystallization process of GST-225 by controlling the baking time at a temperature of 408 K. The reflectance spectra of the metasurface under LCP and RCP illumination are measured after the sample is baked at 408 K for five minutes and cooled to room temperature [33]. This process is repeated until the reflection spectra remain unchanged without any wavelength shift. Figure 4(a) depicts the experimental absorption spectra at the baking time of 0, 5, 10 and 15 minutes, respectively. It is clear that the chiral resonance wavelength gradually shifts from 2.33 μm to 2.46 μm, 2.55 μm and 2.58 μm as the baking time increases, manifesting the dynamic tuning of the GST-based chiral metasurface caused by the permittivity change of GST-225 spacer layer during thermally induced phase transition from the amorphous state to the crystalline state. During the GST crystallization process, strong absorption of LCP light maintains while the absorption of RCP light is kept at a low level. The chiral resonance wavelengths and CD values

Optics EXPRESS

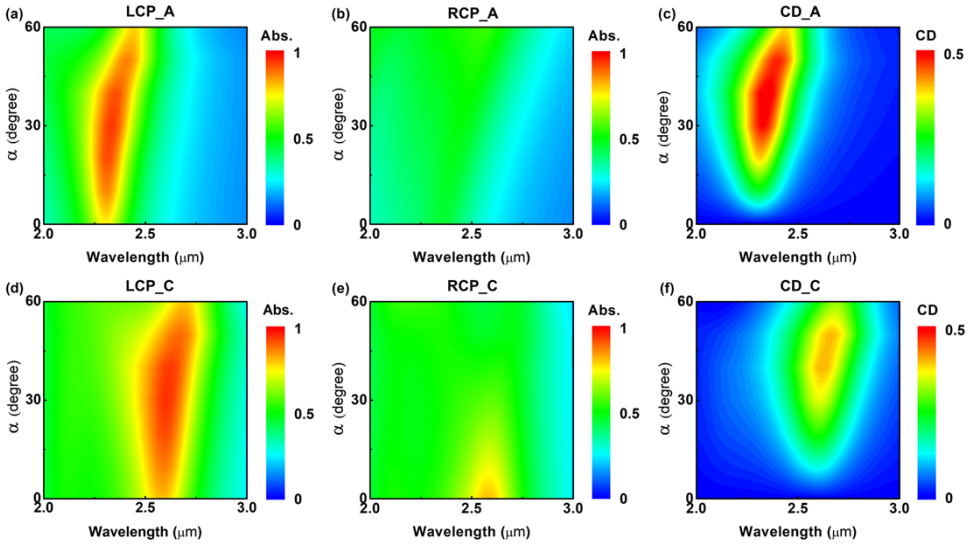

Fig. 3. Simulated absorption spectrum mapping of the metasurface under LCP and RCP illumination by varying α from 0° to 60° (a), (b) at the amorphous state and (d), (e) the crystalline state. (c), (f) Simulated CD spectrum mapping for the chiral metasurface as a function of α from 0° to 60° at both phase states.

are plotted in Fig. 4(c) as a function of baking time, showing a linear wavelength tuning for the chiral metasurface with an almost constant CD value, which reveals the potential application of the chiral metasurface in tunable chiral switching. The simulated absorption spectra, resonance wavelengths and CD values presented in Fig. 4(b) and 4(c) are in good agreement with the experimental results.

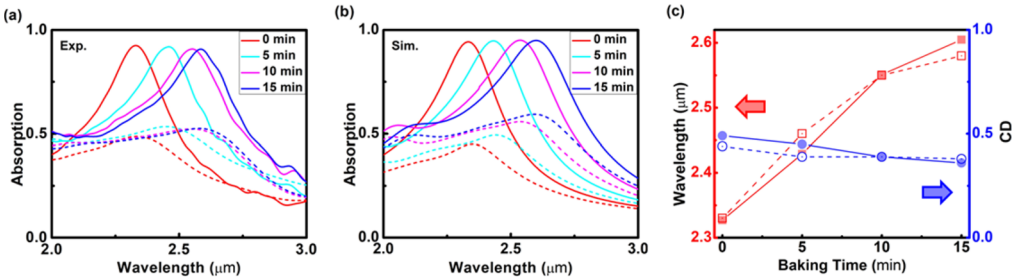

Fig. 4. (a) Measured and (b) simulated absorption spectra of the metasurface at different baking times at 408 K during the GST crystallization process. The solid (dashed) lines represent the spectra under LCP (RCP) incidence. (c) Chiral resonance wavelengths and CD values for different baking times. The hollow points are experiment data, while the solid points are from simulation.

The chiral plasmonic resonant modes under LCP and RCP illumination are analyzed using COMSOL numerical simulations to understand the mechanism of the chiroptical responses from the chiral metasurfaces. Figure 5(a) shows the normalized electric field |E| distributions at the interface between the GST layer and the alumina layer in the X-Y plane. The incident electric field |E| of 2.45×10^5 V/m is used in the simulation for both LCP and RCP light. The coupling of the LCP incident light to the plasmon resonance mode of the parallelogram-shaped resonator is stronger than that of RCP incident light, indicating the high absorption of LCP light and a large CD

Optics EXPRESS

in absorption. The normalized electric field |E| distributions in the cross-sectional X-Z plane are further examined in Fig. 5(b). Under LCP incidence, the electric field is concentrated around the edges of the metallic parallelogram structure and in the alumina capping layer, and also extends into the GST layer. On the contrary, the electric field is much weaker under RCP incidence. The distributions of magnetic field |H| and displacement current J_D in the cross-sectional plane are also plotted in Fig. 5(c). It shows that magnetic dipole modes are strongly excited in the GST spacer layer for LCP light, compared to the RCP case. The displacement current forms three circulating current loops around the magnetic dipole modes, which leads to the strong optical absorption for LCP light.

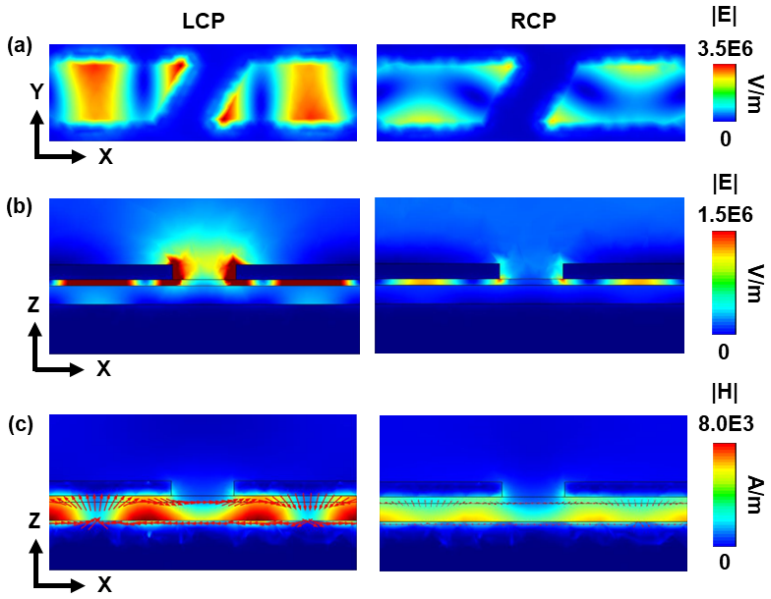

Fig. 5. (a) Simulated electric field |E| distribution at the interface of GST layer and alumina layer under LCP and RCP illumination at the resonance wavelength. (b) Simulated electric field |E| distribution along the cross-sectional plane. (c) Simulated magnetic field |H| and displacement current J_D distributions along the cross-sectional plane. The red arrows represent the direction and intensity of displacement current.

The demonstrated GST-based chiral metasurface utilizes the thermally induced phase transition of GST by high-temperature baking to achieve wavelength-tunable absorption spectra with high CD values. Moreover, the phase transition of GST in the chiral metasurface can also be realized by the photothermal effect depending on the circular polarization of the incident light. The stronger absorption in chiral metasurface under LCP incidence will lead to a higher temperature increase in the GST layer, compared to the RCP case. Therefore, the temperature distributions in the chiral metasurface through the photothermal heat generation at different incident optical power densities are investigated by solving the heat transfer equation $C_p\rho\partial T/\partial t + \nabla \cdot (-k\nabla T) = q$ through COMSOL simulations, where q is the heat generation density calculated by $q = (\omega/2)\,\mathrm{Im}[\varepsilon(\omega)]\varepsilon_0|\mathrm{E}|^2$, T is the temperature, C_p, ρ and k are the specific heat capacity, density and thermal conductivity, respectively. LCP and RCP light is incident from the top boundary of the unit cell, and the thermal insulation boundary conditions along the X and Y directions are applied. In addition, a 100 μm silicon substrate is set underneath the bottom aluminum layer, and constant-temperature boundary conditions are applied at both the top and bottom boundaries at room temperature 300 K [34]. The thermal parameters of different materials used in the simulations are listed in Table 1 [35–37]. Figure 6(a) plots the maximum temperatures

Optics EXPRESS

obtained at the interface between the GST layer and the alumina layer under LCP and RCP incidence at different optical power densities, showing a linear power-dependent temperature increase. When the optical power density is between 62 and 124 μW/μm^2, the temperature of the GST layer exceeds the phase transition temperature of 393 K for LCP light, indicating the phase transition of GST can be induced by the LCP light but the phase transition is not triggered by the RCP light. It is noted that infrared fiber lasers emitting in the 2 - 3 μm spectral region with tens of mW output power are capable of delivering enough optical power density predicted above for the photothermal-induced transition. Figures 6(b) and 6(c) present the temperature distributions at the interface between the GST layer and the alumina layer under circularly polarized illumination with an incident optical power density of 80 μW/μm^2, illustrating that the high CD in absorption of the chiral metasurface leads to a large difference in temperature between LCP and RCP light. For LCP light, the interface temperature increases significantly up to 420 K, exceeding the phase transition temperature of GST. In contrast, the low optical absorption of the RCP light leads to the interface temperature of only 360 K, which is below the phase transition point. These results infer that photothermally induced phase transition in GST can be controlled by the selection of circular polarization and optical power density of the incident light.

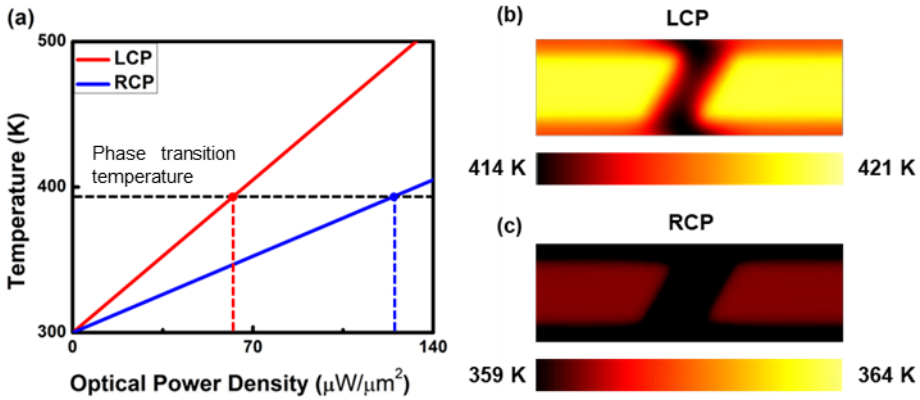

Fig. 6. (a) The photothermally induced maximum temperature at the interface between the GST layer and the alumina layer under LCP and RCP illumination with different optical power densities. The horizontal black dashed line represents the phase transition temperature of 393 K in GST-225. Red (blue) dashed line refers to the required optical power density of LCP (RCP) incident light to reach the phase transition temperature in the GST layer. (b), (c) Simulated temperature distributions at the interface of the GST layer and the alumina layer under LCP and RCP illumination at the chiral resonance wavelength with optical power density of 80 μW/μm^2.

Table 1. Physical properties of materials for heat transfer analysis

	ρ (kg/m^3)	C_p (J/kg·K)	k (W/m·K)
Aluminum	2700	900	240
GST-225	5870	202	0.2
Alumina	3970	765	1.6
Silicon	2330	712	148
Air	1	353	0.03

Optics EXPRESS

3. Conclusion

In summary, wavelength-tunable infrared chiral metasurfaces with parallelogram-shaped resonators based on phase-change material GST-225 have been designed and demonstrated. The chiral resonance wavelength gradually shifts from 2.33 μm to 2.58 μm while the CD in absorption is maintained at the same level as the GST layer changes from the amorphous state to the crystalline state by controlling the baking time of the metasurface above the phase transition temperature. The distributions of electromagnetic fields and displacement current under LCP and RCP illumination have been analyzed to study the chiroptical responses of the metasurface. Furthermore, temperature distributions in the chiral metasurface through photothermal heat generation are simulated to show the large temperature difference in GST layer between LCP and RCP incidence, which allows the control of the phase transition in GST by the selected circular polarization and optical power density of the incident light. This work will not only promote the development of adaptive and active metasurfaces by using the phase-change materials, but also provide the opportunity of circular polarization controlled dynamic modulation in switchable metasurfaces. The dynamic modulation and switching speed of the chiral metasurfaces based on photothermally induced GST phase change can be in the order of picoseconds to nanoseconds, depending on the laser pulse duration and intensity, as well as thermal conductance of materials [38,39]. The demonstrated results in phase-change chiral metasurface will greatly advance future applications in optical switching, thermal imaging, chiral sensing and holographic imaging [40–42].

Funding. National Science Foundation (ECCS-2230069, ECCS-2230071, ECCS-2204163); U.S. Department of Energy (DE-AC02-06CH11357).

Acknowledgments. Work performed at the Center for Nanoscale Materials, a U.S. Department of Energy Office of Science User Facility, was supported by the U.S. DOE, Office of Basic Energy Sciences, under Contract No. DE-AC02-06CH11357. The authors acknowledge the support from the Intelligent Systems Center and the facility support from the Materials Research Center at Missouri S&T.

Disclosures. The authors declare no conflicts of interest.

Data availability. Data underlying the results presented in this paper are not publicly available at this time but may be obtained from the authors upon reasonable request.

References

1. S. Adhikari and M. Orrit, "Optically Probing the Chirality of Single Plasmonic Nanostructures and of Single Molecules: Potential and Obstacles," ACS Photonics **9**(11), 3486–3497 (2022).
2. A. Cabre, X. Verdaguer, and A. Riera, "Recent Advances in the Enantioselective Synthesis of Chiral Amines via Transition Metal-Catalyzed Asymmetric Hydrogenation," Chem. Rev. **122**(1), 269–339 (2022).
3. Y. Chen, X. Yang, and J. Gao, "Spin-controlled wavefront shaping with plasmonic chiral geometric metasurfaces," Light: Sci. Appl. **7**(1), 84 (2018).
4. Y. Y. Lee, R. M. Kim, S. W. Im, M. Balamurugan, and K. T. Nam, "Plasmonic metamaterials for chiral sensing applications," Nanoscale **12**(1), 58–66 (2020).
5. W. Li, Z. J. Coppens, L. V. Besteiro, W. Wang, A. O. Govorov, and J. Valentine, "Circularly polarized light detection with hot electrons in chiral plasmonic metamaterials," Nat. Commun. **6**(1), 8379 (2015).
6. L. A. Warning, A. R. Miandashti, L. A. McCarthy, Q. Zhang, C. F. Landes, and S. Link, "Nanophotonic Approaches for Chirality Sensing," ACS Nano **15**(10), 15538–15566 (2021).
7. A. Alvarez-Fernandez, C. Cummins, M. Saba, U. Steiner, G. Fleury, V. Ponsinet, and S. Guldin, "Block copolymer directed metamaterials and metasurfaces for novel optical devices," Adv. Opt. Mater. **9**(16), 2100175 (2021).
8. L. Ouyang, W. Wang, D. Rosenmann, D. A. Czaplewski, J. Gao, and X. Yang, "Near-infrared chiral plasmonic metasurface absorbers," Opt. Express **26**(24), 31484–31489 (2018).
9. Y. Chen, J. Gao, and X. Yang, "Chiral grayscale imaging with plasmonic metasurfaces of stepped nanoapertures," Adv. Opt. Mater. **7**(6), 1801467 (2019).
10. S. Droulias and L. Bougas, "Absolute chiral sensing in dielectric metasurfaces using signal reversals," Nano Lett. **20**(8), 5960–5966 (2020).
11. E. Mohammadi, K. Tsakmakidis, A. N. Askarpour, P. Dehkhoda, A. Tavakoli, and H. Altug, "Nanophotonic platforms for enhanced chiral sensing," ACS Photonics **5**(7), 2669–2675 (2018).
12. Y. Chen, X. Yang, and J. Gao, "3D Janus plasmonic helical nanoapertures for polarization-encrypted data storage," Light: Sci. Appl. **8**(1), 45 (2019).

Optics EXPRESS

13. C. U. Hail, A. K. U. Michel, D. Poulikakos, and H. Eghlidi, "Optical metasurfaces: evolving from passive to adaptive," Adv. Opt. Mater. **7**(14), 1801786 (2019).
14. A. K. U. Michel, M. Wuttig, and T. Taubner, "Design parameters for phase-change materials for nanostructure resonance tuning," Adv. Opt. Mater. **5**(18), 1700261 (2017).
15. L. Long, S. Taylor, and L. Wang, "Enhanced infrared emission by thermally switching the excitation of magnetic polariton with scalable microstructured VO2 metasurfaces," ACS Photonics **7**(8), 2219–2227 (2020).
16. F. Ding, S. Zhong, and S. I. Bozhevolnyi, "Vanadium dioxide integrated metasurfaces with switchable functionalities at terahertz frequencies," Adv. Opt. Mater. **6**(9), 1701204 (2018).
17. C.-Y. Hwang, G. H. Kim, J.-H. Yang, C.-S. Hwang, S. M. Cho, W.-J. Lee, J.-E. Pi, J. H. Choi, K. Choi, and H.-O. Kim, "Rewritable full-color computer-generated holograms based on color-selective diffractive optical components including phase-change materials," Nanoscale **10**(46), 21648–21655 (2018).
18. M. Zhang, M. Pu, F. Zhang, Y. Guo, Q. He, X. Ma, Y. Huang, X. Li, H. Yu, and X. Luo, "Plasmonic metasurfaces for switchable photonic spin–orbit interactions based on phase change materials," Adv. Sci. **5**(10), 1800835 (2018).
19. W. Bai, P. Yang, J. Huang, D. Chen, J. Zhang, Z. Zhang, J. Yang, and B. Xu, "Near-infrared tunable metalens based on phase change material Ge2Sb2Te5," Sci. Rep. **9**(1), 5368 (2019).
20. M. Y. Shalaginov, S. An, Y. Zhang, F. Yang, P. Su, V. Liberman, J. B. Chou, C. M. Roberts, M. Kang, and C. Rios, "Reconfigurable all-dielectric metalens with diffraction-limited performance," Nat. Commun. **12**(1), 1225 (2021).
21. W. Senbua, J. Mearnchu, and J. Wichitwechkarn, "Easy-to-use and reliable absorbance-based MPH-GST biosensor for the detection of methyl parathion pesticide," Biotechnol. Rep. **27**, e00495 (2020).
22. K. V. Sreekanth, Q. Ouyang, S. Sreejith, S. Zeng, W. Lishu, E. Ilker, W. Dong, M. ElKabbash, Y. Ting, and C. T. Lim, "Phase-change-material-based low-loss visible-frequency hyperbolic metamaterials for ultrasensitive label-free biosensing," Adv. Opt. Mater. **7**(12), 1900081 (2019).
23. M. N. Julian, C. Williams, S. Borg, S. Bartram, and H. J. Kim, "Reversible optical tuning of GeSbTe phase-change metasurface spectral filters for mid-wave infrared imaging," Optica **7**(7), 746–754 (2020).
24. Y. Qu, Q. Li, L. Cai, M. Pan, P. Ghosh, K. Du, and M. Qiu, "Thermal camouflage based on the phase-changing material GST," Light: Sci. Appl. **7**(1), 26 (2018).
25. D. Kang, Y. Kim, C. Kim, and M. Lee, "Highly Flexible Infrared Emitter with Spatially Controlled Emissivity for Optical Security," Adv. Mater. Technol. **8**(4), 2200808 (2023).
26. B. Gholipour, J. Zhang, K. F. MacDonald, D. W. Hewak, and N. I. Zheludev, "An all-optical, non-volatile, bidirectional, phase-change meta-switch," Adv. Mater. **25**(22), 3050–3054 (2013).
27. S. A. Khan, N. Z. Khan, Y. Xie, M. T. Abbas, M. Rauf, I. Mehmood, M. Runowski, S. Agathopoulos, and J. Zhu, "Optical sensing by metamaterials and metasurfaces: from physics to biomolecule detection," Adv. Opt. Mater. **10**(18), 2200500 (2022).
28. B. Tang, Z. Y. Li, E. Palacios, Z. H. Liu, S. Butun, and K. Aydin, "Chiral-selective plasmonic metasurface absorbers operating at visible frequencies," IEEE Photonics Technol. Lett. **29**(3), 295–298 (2017).
29. M. A. Luong, D. Wen, E. Rahier, N. Ratel Ramond, B. Pécassou, Y. Le Friec, D. Benoit, and A. Claverie, "Impact of nitrogen on the crystallization and microstructure of Ge-rich GeSbTe alloys," Phys. Status Solidi RRL **15**(3), 2000443 (2021).
30. X. Zeng, D. Rosenmann, D. A. Czaplewski, J. Gao, and X. Yang, "Mid-infrared chiral metasurface absorbers with split-ellipse structures," Opt. Commun. **525**, 128854 (2022).
31. A. D. Rakić, A. B. Djurišić, J. M. Elazar, and M. L. Majewski, "Optical properties of metallic films for vertical-cavity optoelectronic devices," Appl. Opt. **37**(22), 5271–5283 (1998).
32. K. Shportko, S. Kremers, M. Woda, D. Lencer, J. Robertson, and M. Wuttig, "Resonant bonding in crystalline phase-change materials," Nat. Mater. **7**(8), 653–658 (2008).
33. Y. Chen, T.-S. Kao, B. Ng, X. Li, X. Luo, B. Luk'Yanchuk, S. Maier, and M. Hong, "Hybrid phase-change plasmonic crystals for active tuning of lattice resonances," Opt. Express **21**(11), 13691–13698 (2013).
34. Z. Li, L. Stan, D. A. Czaplewski, X. Yang, and J. Gao, "Wavelength-selective mid-infrared metamaterial absorbers with multiple tungsten cross resonators," Opt. Express **26**(5), 5616–5631 (2018).
35. D. Haemmerich, "Mathematical modeling of heat transfer in biological tissues (bioheat transfer)," in *Principles and Technologies for Electromagnetic Energy Based Therapies* (Elsevier, 2022), pp. 1–24.
36. M. S. Mahmud, D. Rosenmann, D. A. Czaplewski, J. Gao, and X. Yang, "Chiral plasmonic metasurface absorbers in the mid-infrared wavelength range," Opt. Lett. **45**(19), 5372–5375 (2020).
37. K. Aryana, J. T. Gaskins, J. Nag, D. A. Stewart, Z. Bai, S. Mukhopadhyay, J. C. Read, D. H. Olson, E. R. Hoglund, and J. M. Howe, "Interface controlled thermal resistances of ultra-thin chalcogenide-based phase change memory devices," Nat. Commun. **12**(1), 774 (2021).
38. A. V. Kiselev, V. V. Ionin, A. A. Burtsev, N. N. Eliseev, V. A. Mikhalevsky, N. A. Arkharova, D. N. Khmelenin, and A. A. Lotin, "Dynamics of reversible optical properties switching of Ge2Sb2Te5 thin films at laser-induced phase transitions," Opt. Laser Technol. **147**, 107701 (2022).
39. Q. He, Z. Liu, Y. Lu, G. Ban, H. Tong, Y. Wang, and X. Miao, "Low-loss ultrafast and nonvolatile all-optical switch enabled by all-dielectric phase change materials," iScience **25**(6), 104375 (2022).
40. B. Atorf, H. Mühlenbernd, T. Zentgraf, and H. Kitzerow, "All-optical switching of a dye-doped liquid crystal plasmonic metasurface," Opt. Express **28**(6), 8898–8908 (2020).

Optics EXPRESS

41. S. A. Mann, N. Nookala, S. C. Johnson, M. Cotrufo, A. Mekawy, J. F. Klem, I. Brener, M. B. Raschke, A. Alù, and M. A. Belkin, "Ultrafast optical switching and power limiting in intersubband polaritonic metasurfaces," Optica **8**(5), 606–613 (2021).
42. Q. Wang, E. Plum, Q. Yang, X. Zhang, Q. Xu, Y. Xu, J. Han, and W. Zhang, "Reflective chiral meta-holography: multiplexing holograms for circularly polarized waves," Light: Sci. Appl. **7**(1), 25 (2018).